In-situ synchrotron x-ray radiography investigations of water transport in PEM fuel cells

Ingo Manke[1,2], Christoph Hartnig[3], Nikolay Kardjilov[2], Heinrich Riesemeier[4], Jürgen Goebbels[4], John Banhart[1,2]

[1]Institute of Materials Science and Technology, Technical University Berlin, Hardenbergstr. 36, 10623 Berlin, Germany, [2]Helmholtz Centre Berlin, Glienicker Str. 100, 14109 Berlin, Germany, [3]Centre for Solar Energy and Hydrogen Research (ZSW), Baden-Württemberg, Helmholtzstraße 8, 89081 Ulm, Germany, [4]Federal Institute for Materials Research and Testing, Unter den Eichen 87, 12205 Berlin, Germany

Abstract

Water transport in an operating PEM fuel cell was investigated with synchrotron x-ray radiography with a spatial resolution of 3 µm and a temporal resolution of 5 seconds. This method allows for the detection of water accumulations with less than 10 µm diameter. We demonstrate that synchrotron x-ray imaging can dramatically expand the possibilities of imaging with high spatial and time resolution, especially as a complement to neutron radiography. Water transport processes from the first appearance of small water accumulations in the gas diffusion layer to their transport into the channel system were analyzed in situ. Correlations between local effects such as water formation and operating conditions of the whole system, e.g. power variations, were found. A recently described eruptive water transport mechanism is analyzed in detail.

Key words: fuel cell, synchrotron x-ray radiography, imaging, water transport, two-phase flow, gas diffusion layer

1 Introduction

During the past decade, the global demand for energy has exploded, raising the need for highly efficient energy conversion that combines with new technologies to satisfy the need for safe energy supplies [1-3]. Fuel cell technology has the advantage of directly converting chemical energy into electrical and thermal energy without noise or hazardous emissions and contributes to a safe, sustainable energy supply.

Low temperature polymer electrolyte (PEM) fuel cells are the most promising candidates for future applications in mobile and stationary applications [1-3]. In PEM fuel cells, hydrogen and oxygen react to form water and, due to the separation of the anodic and cathodic processes, electrical energy. Protons migrate through the membrane and recombine with oxygen on the surface of the cathodic catalyst where oxygen is reduced and forms water (see schematic drawing of a typical cross section through a PEM fuel cell in Fig. 1).

In PEM fuel cells, liquid water plays a crucial role. On the one hand, only the wet membrane is proton conductive; a dry polymer membrane changes its structure and the conductivity of the membrane collapses. On the other hand, flooding is a significant source of power losses during fuel cell operation [1-5]. If the catalyst layer and the adjacent gas diffusion layer are filled with liquid water, the transport of reactant and product gases (O_2, H_2 and H_2O) is strongly hindered and the supply of the reactive area, i.e. the catalyst, is reduced. Thus a well-balanced water management, i.e. wet conditions coupled with simultaneous fast transport of product water, at any operating condition is an important aspect of development and, along with the choice of the membrane materials, a major challenge for the efficiency and lifetime of PEM fuel cells [6].

In the past few years, interest in these issues has been increasing continuously and many advances have been made in this field. However, a complete insight into the fundamental processes of liquid water development and transport is still missing, hampering a specific strategy for component development.

Besides the flow field and membrane, the GDL is the most important component as it is responsible for wetting the membrane as well as for the fast transfer of liquid water from the catalyst to the flow field channel. The most commonly used GDL materials consist of carbon fibers that are a few µm thick and are more or less arbitrarily distributed. This results in typical porosities of 60-80% with pore sizes of a few 10 µm in diameter. The carbon fibers are normally coated with a hydrophobic material such as teflon in order to prevent the development of a thin film of liquid water at the catalyst. The structure of a sophisticated GDL material can be very complex and varies depending on the required properties for the corresponding fuel cell. However, the high complexity of the interaction between environmental conditions inside a fuel cell and materials properties do not allow for a sufficiently detailed prediction of water development and transport. Development of advanced models that describe the water transport under any operating condition is therefore desirable. For this task it is essential to obtain insights into the fundamental mechanisms of water transport in the GDL pore network that act as a channel system for the flowing liquid water.

Although progresses in water transport simulations were achieved [7-23], until now only a few techniques for in-situ investigations have been available. Preparation of special fuel cell setups, e.g. with optically transparent components, is possible [24-26] but introduces distortions into the system and provides only limited access to the water transport inside the GDL which is not transparent. In the past, neutron radiography has been found to be very useful for in-situ investigations of the transport of water in the flowfields and the water saturation in the GDLs [27-41]. The high penetration depths into many materials – especially metals – and the comparable high attenuation coefficient of hydrogen makes neutron imaging an excellent technique for investigation of the distribution of hydrogen-containing materials, e.g. behind metallic components [42,43], in general. For investigations of small fuel cells magnetic resonance imaging was applied very successfully [44-46].

One of the main drawbacks of neutron imaging is the rather low spatial resolution of typically 100-250 µm [42]. Recent achievements in detector development enable spatial resolutions down to about 20-50 µm [36,37]. However, the rather low neutron flux of less than $10^6 mm^{-2} s^{-1}$ available even at the best neutron sources limits the signal-to-noise ratio and makes long exposure times of typically 5-30 min necessary for high resolution measurements. This is not sufficient for fast investigations of the water formation and transport dynamics in the small pores of the GDL or the transition step of water from the GDL to the channel. Even if the spatial resolution is very close to the typical pore sizes of around 10 µm to 50 µm, a time resolution of a few seconds is not achievable.

Imaging instruments at synchrotron x-ray sources do not have these limitations. They are very suitable for investigations of small areas (around a few mm) with a spatial resolution of a few µm. The comparable high x-ray flux, typically between 10^{10} and 10^{12} photons/($mm^2 s$) and sometimes more depending on the instrument setup, provides sufficient signal-to-noise-ratio even at short exposure times of a few seconds. However, x-rays are strongly attenuated by metals and other components used in fuel cells.

In this paper investigations on the water transport behavior in the GDL of an operating fuel cell are shown. A spatial resolution of 3 µm and a time resolution of 5 s were achieved by using synchrotron x-ray radiography. Both the resolution and the ability to perform measurements in an (almost) unmodified and undisturbed system exhibit a unique method to gain a realistic image of the transport and production of liquid water [47, 48].

2 Experimental setup

2.1 Synchrotron x-ray imaging facility

The experiments were performed at the tomography facility of the Helmholtz Centre Berlin (formerly Hahn-Meitner Institute Berlin) and the Federal Institute of Materials Research and Testing (BAM), the BAMline, which is located at the synchrotron source BESSY in Berlin (Germany) [49]. A W-Si

multilayer monochromator with an energy resolution of about $\Delta E/E = 10^{-2}$ was used to obtain a monochromatic x-ray beam with an energy of 13 keV. This energy was chosen to provide good transmission through the prepared fuel cell (for details see below) while maintaining sufficient sensitivity to water, i.e. the reduction in transmission by the water is strong enough to visualize it without the use of any contrast medium despite the strong absorption of the other fuel cell components .A 2048x2048 pixel^2 camera setup (Princeton VersArray 2048B with a Gadox scintillator screen) was used to capture image area sizes up to 7x7 mm^2 with pixel sizes between 1.5 and 3.5 µm and a physical spatial resolution of typically 3-8 µm. The measurement time per image was around 4.8 s, consisting of 1 s exposure time and 3.8 s read-out time. In this way, a good compromise between measurement time and signal-to-noise ratio was achieved. A schematic drawing of the radiography setup is shown in Fig. 2.

The fuel cell was mounted on translation and rotation stages. In this way, the region of interest could be selected and the cell could also be driven to the side for the measurement of flat field images, which are taken to eliminate inhomogenities in the beam intensity distribution. In the normalization step, all radiographic images are divided by a corresponding flat field image.

2.2 Fuel cells

A single cell setup was used for all measurements; the anodic and cathodic threefold serpentine flow fields with 1 mm wide channels and ribs and an active area of 100 cm^2 were machined in separate blank graphite composite plates (SGL Carbon) with the cooling water distribution field grafted into the cathodic part. GORE PRIMEA 5620 membrane electrode assemblies with a platinum loading of 0.3 mg/cm^2 on the anode and 0.4 mg/cm^2 on the cathode side were employed [50]. SGL Carbon 10 BB material was used as the GDL [50]. The operating cell was investigated through small holes of 8 mm diameter in the metallic end-plates of the cell that were carefully sealed. Liquid water from the cooling bypassed these positions. The flow field and the other components remained completely unmodified. Thus, the slight modification of

the housing does not influence the thermal and electrical conductivity of the components and the water development and transport in the cell.

3 Experimental results

A typical raw image as obtained during the experiment is shown in Fig. 3a. The flow field channels on the cathode and anode side can be seen. The best way to derive the water distribution from this image is normalization with respect to a radiogram of a “dry” cell. This way, the pure liquid water distribution is obtained (Fig. 3b). The white spots in the image can be assigned to water clusters in GDL material and flow field channels (white arrows). In most cases, the image used for normalization is not completely “dry” - a few water droplets might remain in the GDL or even the channels. These can be identified as black areas in this image (black arrows). The reason for this is that the initial image of a dry cell cannot always be used for all measurements due to mechanical creep and thermal expansion of the setup which slightly changes the location of the cell. These effects make it impossible to keep the setup at a constant position within the required accuracy of around 1 µm for long periods of time. In the example shown in Fig. 3b, a large (around 1 mm diameter) water droplet was located in the anodic flow field channel and was removed after the fuel cell was started again causing “negative” water accumulations in the normalized radiogram. “Negative” means in this context that there is less water at this specific location in an operating cell than in the “dry” cell.

Figure 4 compares neutron and synchrotron x-ray radiography for fuel cell research in order to demonstrate the complementarity of the techniques. Neutron radiography is able to map the whole active area of the cell in the order of 100 to 200 cm^2. The metallic and carbon components can be penetrated by the neutrons at all locations. On the other side, synchrotron x-ray radiography is employed to investigate one part of the cell with very high spatial resolution.

Since the advantages of neutron imaging are well known, we would like to demonstrate the specific strengths of synchrotron x-ray radiography in more

detail. Figure 5 shows a comparison of the achievable spatial resolution between synchrotron x-ray and neutron radiography. All images were taken from the same area of the same fuel cell. The exposure time was 1 s for the synchrotron x-ray radiographic images and 10 s for the neutron radiographic images. Read-out time was 3.8 s in both cases. Although at long exposure times of around a few minutes image quality is excellent and important information about the saturation of the GDL and its distribution can be obtained [36,37], a detailed analysis of the exact water formation in the GDL pores and the correlated fast transport processes within the GDL is a challenge normally beyond the potential of neutron imaging. This can be derived from the neutron radiography image shown in Fig. 5a), which was taken with an exposure time of only 10 s: Some small droplets in the channels can be seen and the overall saturation in the GDL might be derived from the image. However, it is practically impossible to see the small water accumulations in the GDL pores. Although a maximum achievable spatial resolution of around 70 µm was possible with this setup the modulation transfer function gives a spatial resolution in the range of around 150 µm in the shown image caused by the limited count rate due to the short exposure time. The rather low spatial resolution is mainly caused by the weak signal and correlated low signal-to-noise ratio in fast measurements. Image quality cannot be further increased by increasing the spatial resolution.

This image is now compared to a synchrotron x-ray radiogram in Fig 5b. Enlargements of the areas marked in black in Fig. 5 a and b are displayed in Fig. 5 c and d, respectively. The differences between neutron and synchrotron x-ray radiography are obvious. In the synchrotron x-ray radiograms the water droplets are displayed with such a high accuracy that even details like the droplets' contact angle at the channel-material surface and the droplets' orientation in space can be determined. In addition, fine water accumulations in the GDL pores with only a few µm in diameter can be seen [see arrows in Fig. 5 d)]. This comparison clearly demonstrates the advantage of synchrotron x-ray radiography for fast and high resolution measurements.

It should be mentioned that this method also has its limitations: if, for example, some metallic components such as a metal flow field are in the line of the beam

the low x-ray energy used here is not sufficient to penetrate the fuel cell. On the other hand, at higher x-ray energies, where metals can be penetrated easily, the attenuation of water is too small; limitations in the signal to noise ratio then prevent the clear visualization of water. The following investigations demonstrate the high potential of synchrotron x-ray radiography for visualization of water clusters in GDL materials.

Fig. 6 a) shows the evolution of liquid water accumulations in the GDL. Additionally, an enlargement of the area marked in white is given in Fig. 6 b). The fuel cell was started at almost dry condition. The time interval between the images was 81.6 s, after which some water accumulations in the GDL appear. These first accumulations start beneath the land (rib) of the flow field. These initial spots of liquid water formation are located beneath the land (ribs) of the flow field. Hardly any water can be seen in the GDL beneath the channel. However, inside the channels a few water droplets can be found at the channel edges. After 2 x 81.6 s the size and amount of the water accumulations increased. After about 10 min. (7 x 81.6s) almost stationary conditions – near equilibrium – are reached and the water saturation does not increase any more.

Along the black rectangle in Fig. 6a (image at the bottom right) horizontal cross sections were taken (approx. 100 horizontal lines were summed up) and the intensities are displayed as line graphs in Fig. 7. As mentioned above, water accumulates first in the GDL below the land. Inside the channel, only a few water droplets at the side of the flow field channels were found.

An interesting feature is the fast droplet building in the flow field channel. The white arrows in Fig. 6a mark the position of such a droplet formation event in the flowfield channel. These processes do not occur completely arbitrarily, but have a specific repetition rate that is correlated with the operating conditions of the fuel cell. This will be shown in the next example where the water transport behavior on a much shorter time scale is investigated.

Figure 8a shows again the same area in the fuel cell, but with smaller time steps of 4.8 s (the time resolution). At first, water has accumulated in the GDL pores (black spots disappear while more white spots appear). After the

accumulation reached a specific level, the water was expelled into the channels where it formed two droplets (white arrows). As can be seen, the droplet formation occurs from one image to the other within a time interval below the time resolution of 4.8 s. The droplets evaporate within the next 10-15 s. A 100% relative humidity has not been reached and the droplets can evaporate.

Fig. 9 shows a schematic drawing of this eruptive transport. Firstly, water accumulates in the pores of the GDL until a specific amount is reached. Then, within a few seconds or even less, one part of the water is expelled and forms a droplet at the channel wall.

The whole sequence of Fig. 8a repeats again after some time is passed. The process is periodic with an almost constant period time. This is demonstrated in Fig. 8b. This image series shows the same location 105.6 s later. It is remarkable that the images are almost identical to those in Fig. 8a. The overall periodicity is kept during the entire observation time of more than 45 min. This water transport mechanism is very sensitive to changes in the operating parameters as will be shown in the next example.

The image series in Fig. 10 was taken during transition from one operating condition to another. The series shows one of the eruptive water transport channels with time intervals of 4.8 s between succeeding images. Each eruptive event is marked by a white arrow. At the beginning of this series, specific operating conditions have been set (u_C=25%, u_A=95%, i_0=500 mA/cm^2) from which one of the parameters – the anodic utilization rate u_A – was slightly changed from 95 % to 97.5 %. The system needs some time before changes in the operating parameters affect the water transport behavior as can be derived from Fig. 10. At first, the repetition time of the eruption cycle was about 40 ± 5 s. After around 200 s (40 images), the repetition time decreases slowly to about 25 ± 5 s.

In addition, the water eruption behavior was altered. Beginning from the cycle marked by a white circle, the droplet does not appear immediately with maximum size but seems to grow over a time scale of around 10s to 15 s. Then it disappears suddenly. The time scale of only about 5 s seems to be too small for droplet evaporation. It is possible that the droplet size increases to a specific

level where the resistance of the air flow is high enough to drive it away. Alternatively, another droplet wandering through the channel could be the reason (“avalanche” effect).

After about 230 s, a very interesting new effect is observed: a second “transport channel” opens (black arrow) just below the old one and changes the overall water transport behavior, a detailed discussion will be given below.

The periodic behavior of the water droplet eruption (Fig. 8 and 10) can be well illustrated by monitoring the local water thickness at the droplet’s position as a function of time as shown in Fig. 11[a) and b). Each up and down sequence marks an entire cycle of water expulsion into the channel with subsequent evaporation of the water droplet.

The correlation between the water droplet formation in the channel and water agglomerations in the GDL is illustrated in Fig.11 c), where the local water thickness at the marked location in the GDL (see black arrows) was monitored. For comparison, the corresponding water thickness at the droplet position is shown as well and reveals the strong correlation: period times are identical and the water thickness in the GDL is reduced once a droplet in the channel evolves at the same time.

4 Discussion

The observation of the first appearance of water clusters beneath the lands (ribs) of the flow field is in accordance with theoretical predictions, for example by Kulikovsky et al. [51]. The effect can be explained by an interplay of several factors as, e.g., compression of the GDL below the land, leading to a reduced porosity and extended pathway lengths for product and reactant gases.

The observations concerning the eruptive water transport mechanism is in agreement with the recent findings by Djilali et al. [52-55], who used fluorescent imaging to follow the water transport in GDL materials. They found quick ejection of droplets from the GDL very similar to to the findings here. The observation can be explained as follows: water is transported through the paths with least resistance. Due to inhomogenities in the GDL, surface water emerges at preferential locations, e.g. locations with a comparatively large hole in the

fiber network. It should also be mentioned that Owejan et al. found hints for an eruptive water transport using neutron radiography [41].

The opening of a new “transport channel” as indicated in Fig. 10 (green arrow) could be explained by changes in the pressure distribution within the water-filled GDL due to the changed operating parameters [53]. The amount of liquid water produced in the cell strongly depends on several parameters such as the current density i_0 and the utilization rates. A similar observation was also described very recently by Bazilak et al. in ex-situ studies [53]. They found that the process of the building of breakthrough locations is dynamical. For example, they observed that forming a new breakthrough location could cause the old breakthrough location to recede. These findings are now supported by our in-situ investigations.

5 Conclusions

We demonstrated the strength of synchrotron x-ray radiography to study liquid water transport in fuel cells with a high level of detail. Compared to neutron radiography, only a rather small area can be investigated and slight modifications have to be made to the cell. However, synchrotron x-ray radiography represents the only technique for investigations of fast water transport phenomena in the pores of the GDL materials of fuel cells. Thus water accumulations less than 10 µm in diameter were visualized in-situ. In addition, fast processes such as the “eruptive” water droplet expulsion from the GDL into the flow field channels were studied and could help to understand the underlying water transport mechanisms.

Based on these findings, by synchrotron x-ray radiography the development of sophisticated GDL materials and flow fields as well as water transport models in fuel cell research can be significantly affected. In future, spatial and time resolution might be enhanced by at least one order of magnitude. The applied technique opens a variety of possibilities for future material optimization and might serve as basis for simulation purposes.

Acknowledgements:

The research activities were funded by the German Federal Ministry for Education and Science (BMBF) under grant number 03SF0324A and 03SF0324F (RuNPEM).

[1] L. Carrette, K. A. Friedrich, U. Stimming, Fuel Cells **2001**, *1*, 5-38

[2] Wang, C. Y., Two-phase flow and transport, Volume 3, Part 3, pp 337–347 in *Handbook of Fuel Cells - Fundamentals, Technology and Applications* (ISBN: 0-471-49926-9) edited by Wolf Vielstich, Arnold Lamm, Hubert A. Gasteiger, John Wiley & Sons, Ltd, Chichester, 2003

[3] C.Y. Wang, Chem Rev. **2004**, *104*, 4727-4766

[4] S. Litster, N. Djilali, Transport Phenomena in Fuel Cells, WIT Press, Southampton, UK, 2005, p. 175–213.

[5] N. Djilali, P. C. Sui, International Journal of Computational Fluid Dynamics, **2008,** *22*, 115- 33

[6] W. Schmittinger, A. Vahidi, J. Power Sources **2008,** *180*, 1-14

[7] C.-Y. Wang, Chem. Rev. **2004,** *104*, 4727-4766

[8] U. Pasaogullari, C.-Y. Wang, J. Electrochem. Soc. **2004,** *151*, A399-A406

[9] X. Zhu, P.C. Sui and N. Djilali J. Power Sources **2008** *181* 101-115

[10] X. Zhu, P. C. Sui and Ned Djilali, Microfluidics and Nanofluidics **2007,** *4*, 543-555

[11] T. Berning, N. Djilali, J. Electrochem. Soc. **2003**, *150*, A1589-A1598.

[12] R. Eckl, W. Zehtner, C. Leu, U. Wagner, J. Power Sources **2004,** *138*, 137–144

[13] J. Ge, H. Liu, J. Power Sources **2006,** *160*, 413–421

[14] X.D. Xue, K.W.E. Cheng, D. Sutanto, Electrochim. Acta **2006,** *52*, 1135–1144

[15] E. Birgersson, J. Nordlund, M. Vynnycky, C. Picard, G. Lindbergh, J. Electrochem. Soc., **2004,** *151*, A2157-A2172

[16] G. Lin, W. He, T. Van Nguyen, J. Electrochem. Soc. **2004,** *151*, A1999-A2006

[17] V.P. Schulz, J. Becker, A. Wiegmann, P.P. Mukherjee, C.-Y. Wang, J. Electrochem. Soc. **2007,** *154*, B419-B426

[18] D. Natarajan, T. Van Nguyen, *Journal of Power Sources* **2003,** *115*, 66–80

[19] U. Pasaogullari, C.Y. Wang, *J. Electrochem. Soc.* **2005,** *152***,** 380-390

[20] M. Hu, A. Gu, M. Wang, X. Zhu, L. Yu , *Energy Conversion and Management*, **2004,** *45*, 1861-1882

[21] C. Ziegler, H. M. Yu, and J. O. Schumacher, *Journal of The Electrochemical Society*, **2005,** *152*, 1555-1567

[22] P. Berg, K. Promislow, J. St. Pierre, J.,Stumper, and B. Wetton, *Journal of The Electrochemical Society*, **2004,** *151*, 341-353,

[23] J. Nam, M. Kaviany, Int. J. Heat Mass Transfer **2003,** *46*, 4595–4611.

[24] D. Spernjak, A.K. Prasad, S.G. Advani, J. Power Sources **2007,** *170*, 334-344

[25] F.Y. Zhang, X.G. Yang, C.Y. Wang, J. Electrochem. Soc. **2006** *153*, 225-232

[26] K. Tüber, D. Pócza, C. Hebling, J. Power Sources **2003**, *124*, 403–414

[27] M.A. Hickner, N.P. Siegel, K.S. Chen, D.N. McBrayer, D.S. Hussey, D.L. Jacobson, M. Arif, J. Electrochem. Soc. **2006,** *153*, A902-A908

[28] D.L. Ludlow, C.M. Calabrese, S.H. Yu, C.S. Dannehy, D.L. Jacobson, D.S. Hussey, M. Arif, M.K. Jensen, G.A. Eisman, J. Power Sources **2006,** *162*, 271-278

[29] A. Turhan, K. Heller, J.S. Brenizer, M.M. Mench, J. Power Sources **2006,***160*, 1195-1203

[30]J.J. Kowal, A. Turhan, K. Heller, J. Brenizer, M.M. Mench, J. Electrochem. Soc. 2006 *153*, A1971-A1978

[31] D. Kramer, D.; J. Zhang, J.; R. Shimoi, R.;E. Lehmann, E.;A. Wokaun, A.;K. Shinohara, K.; G.G. Scherer, G.G.; Electrochim. Acta **2005** *50*, 2603-2614

[32] J. Zhang, D. Kramer, R. Shimoi, Y. Ono, E. Lehmann, A. Wokaun, K. Shinohara, G.G. Scherer, Electrochim. Acta **2006,** *51*, 2715-2727

[33] Ch. Hartnig, I. Manke, N. Kardjilov, A. Hilger, M. Grünerbel, J. Kaczerowski, J. Banhart, W. Lehnert, Journal of Power Sources **2008,** *176*, 452-459

[34] I. Manke, C. Hartnig, N. Kardjilov, M. Messerschmidt, A. Hilger, M. Strobl, W. Lehnert, J. Banhart, Appl. Phys. Lett. **2008**. *92*, 244101

[35] I. Manke, Ch. Hartnig, M. Grünerbel, J. Kaczerowski, W. Lehnert, N. Kardjilov, A. Hilger, W. Treimer, M. Strobl, J. Banhart, Applied Physics Letters **2007,** *90*, 184101

[36] M. A. Hickner, N. P. Siegel, K. S. Chen, D. S. Hussey D. L. Jacobson, M. Arif, J. Electrochem. Soc., **2008,** *155*, B427-B434

[37] P. Boillat, D. Kramer, B.C. Seyfang, G. Frei, E. Lehmann, G.G. Scherer, A. Wokaun, Y. Ichikawa, Y. Tasaki, K. Shinohara, Electrochem. Commun. **2008** *10*, 546-550

[38] A.B. Geiger, A. Tsukada, E. Lehmann, Vontobel, P., Wokaun, A., Scherer, G.G., *Fuel Cells* **2002,** *2*, 92-98

[39] R.J. Bellows, M.Y. Lin, M. Arif, A.K. Thompson, D. Jacobson, J. Electrochem. Soc. **1999**, *146*, 1099-1103

[40] R.Satija, D.L. Jacobson, M. Arif, S.A. Werner, J. Power Sources **2004**, *129*, 238–245,

[41] J.P. Owejan, T.A. Trabold, D.L. Jacobson, D.R. Baker, D.S. Hussey, M. Arif, Int. J. Heat Mass Transfer **2006**. *49*, 4721-4731

[42] E. Lehmann, N. Kardjilov, in J. Banhart (Ed.): Advanced Tomographic Methods in Materials Research and Engineering, Oxford University Press (2008)

[43] B. Schillinger,E. Lehmann P. Vontobel, Physica B **2000** *276*, 59-62

[44] K.W. Feindel, S.H. Bergens, R.E. Wasylishen, Phys. Chem. Chem. Phys. **2007,** *9*, 1850-1857

[45] K.W. Feindel, S.H. Bergens, R.W. Wasylishen, J. Power Sources **2007,** *173*, 86-95

[46] K.W. Feindel, S.H. Bergens, R.E. Wasylishen, J. Am. Chem. Soc**2006,** *128*, 14192-14199

[47] Ch. Hartnig, I. Manke, R. Kuhn, N. Kardjilov, J. Banhart, W. Lehnert, Appl. Phys. Lett. **2008**, *90*, 134106

[48] I. Manke, Ch. Hartnig, M. Grünerbel, W. Lehnert, N. Kardjilov, A. Haibel, A. Hilger, H. Riesemeier, J. Banhart, Appl. Phys. Lett. **2007,** *90*, 174105

[49] W. Görner, M.P. Hentschel, B.R. Müller, H. Riesemeier, M. Krumrey, G. Ulm, W. Diete, U. Klein and R. Frahm, Nucl. Instr. and Meth. A, **2001**, *703*, 467-468,

[50] Certain trade names and products are mentioned in the text in order to specify the experimental setup and procedure. In no case does such an identification imply recommendation or endorsement nor does it imply that these materials are necessarily the best available for the application.

[51] A.A. Kulikovsky, T. Wüster, A. Egmen, D. Stolten, J. Electrochem. Soc., **2005,** *152*, A1290-A1300

[52] S. Litster, D. Sinton, N. Djilali, J. Power Sources **2006,** *154* 95-105

[53] Bazylak, D. Sinton, N. Djilali. J. Power Sources **2008,** *176,* 240–246

[54] X. Zhu, P.C. Sui, and Ned Djilali, J. Power Sources **2008,** *172,* 287-295

[55] A. Bazylak, D. Sinton, Z.-S. Liu, N. Djilali, Journal of Power Sources **2007**, *163*, 784-792

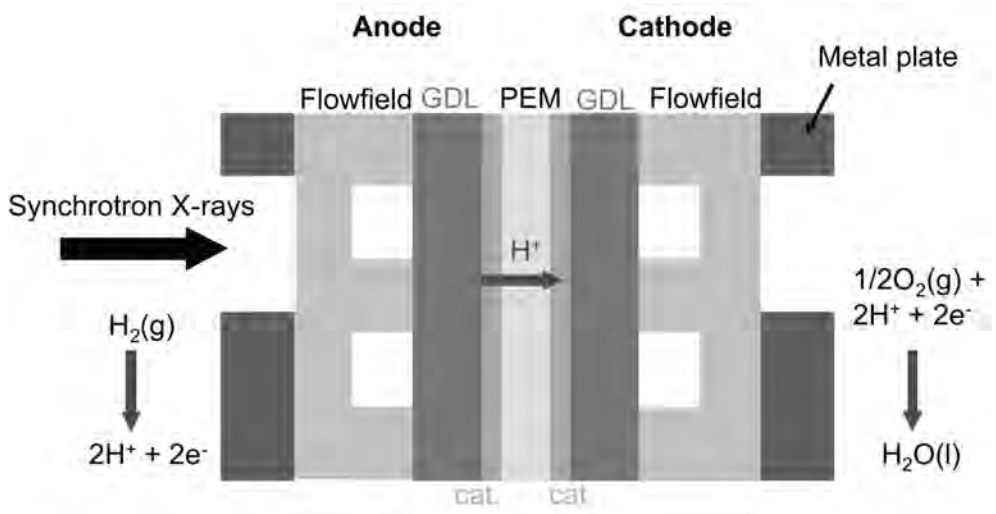

Fig. 1: Schematic drawing of a typical cross-section through a PEM fuel cell.
85x44mm (600 x 600 DPI)

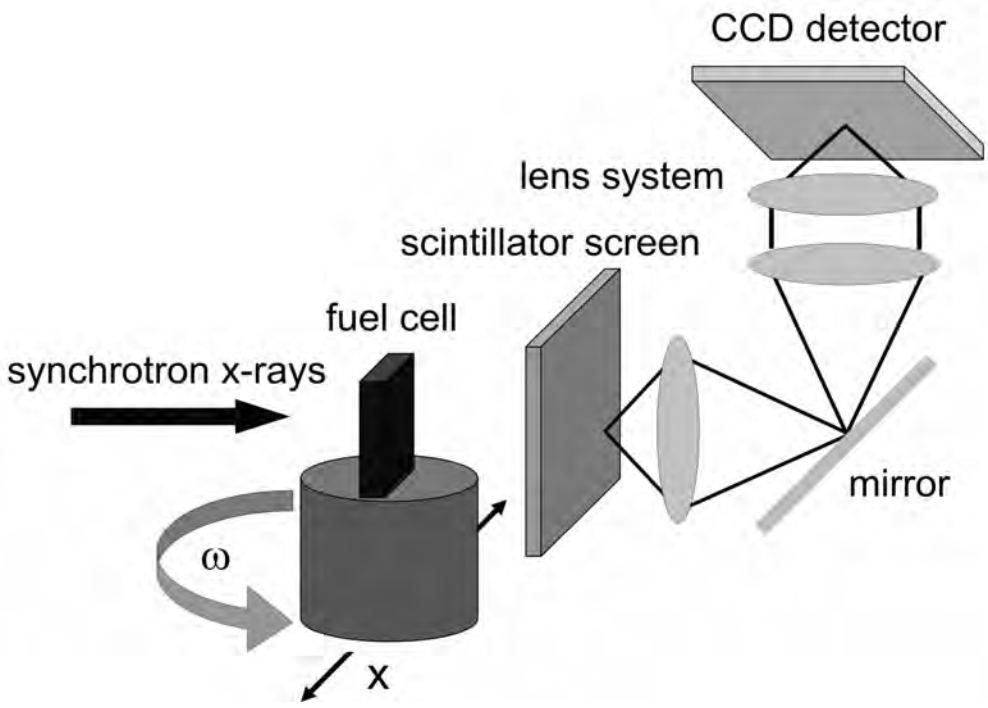

Fig. 2: Schematic drawing of the experimental setup.
85x60mm (600 x 600 DPI)

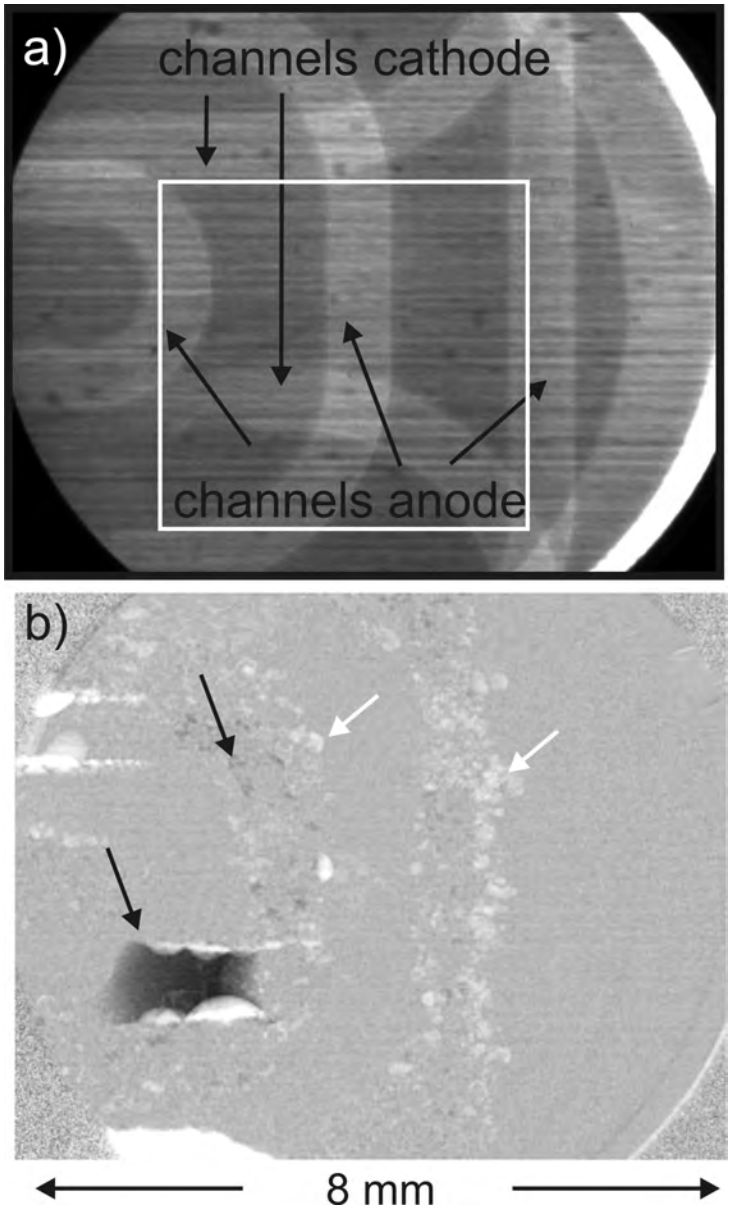

Fig.3: (a) Radiogram as obtained during the experiment. The flow field channels on the cathode and anode side can be seen. (b) A radiogram normalized with respect to a □dry□ cell. The white spots in the image can be assigned to water clusters in GDL material and flow field channels. However, the dry cell still contained some residual water that can be identified as black areas in image (b). In this case, a large droplet was located in the anodic flow field channel and was removed after the fuel cell was started (see text for further description). Thus it can be identified as □negative□ (black) water accumulation.
85x142mm (600 x 600 DPI)

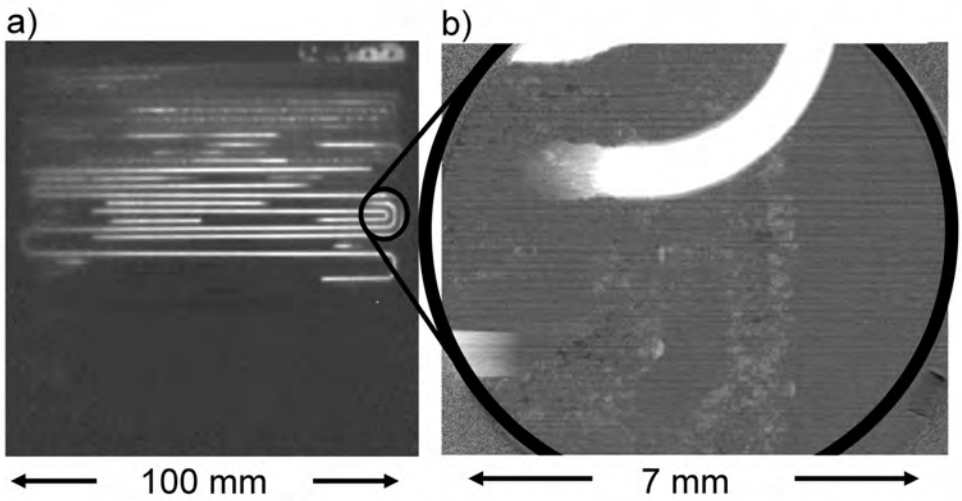

Fig. 4: Complementarity of neutron and synchrotron x-ray radiography: a) Neutron radiogram of the whole active area of a PEM fuel cell and b) synchrotron x-ray radiogram of one part of the same cell with high spatial resolution around a few µm.
85x52mm (600 x 600 DPI)

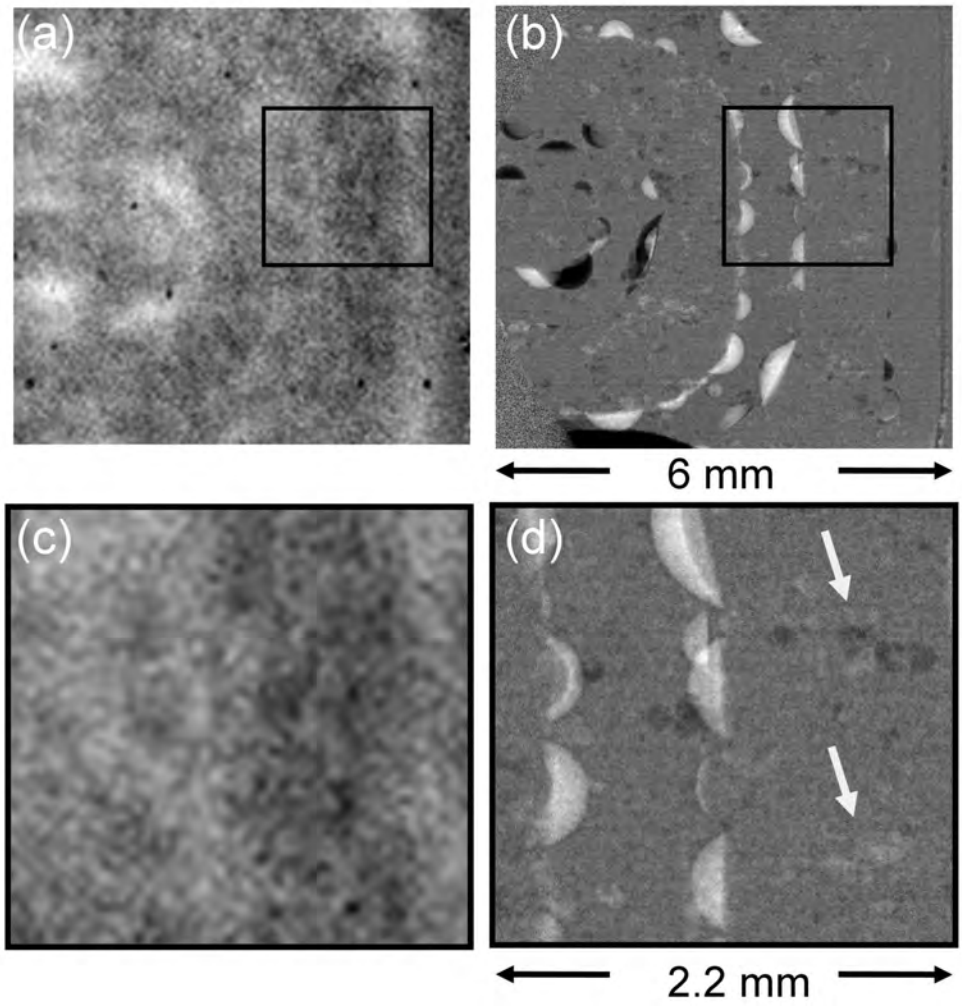

Fig. 5: Comparison of the image qualities obtained with neutron and with synchrotron x-ray radiography for fast measurements with time resolutions around a few seconds. The same location within the same fuel cell was investigated by a) neutron radiography and b) synchrotron x-ray radiography. Corresponding enlargements of the black marked areas in a) and b) are shown in c) and d), respectively.
85x87mm (600 x 600 DPI)

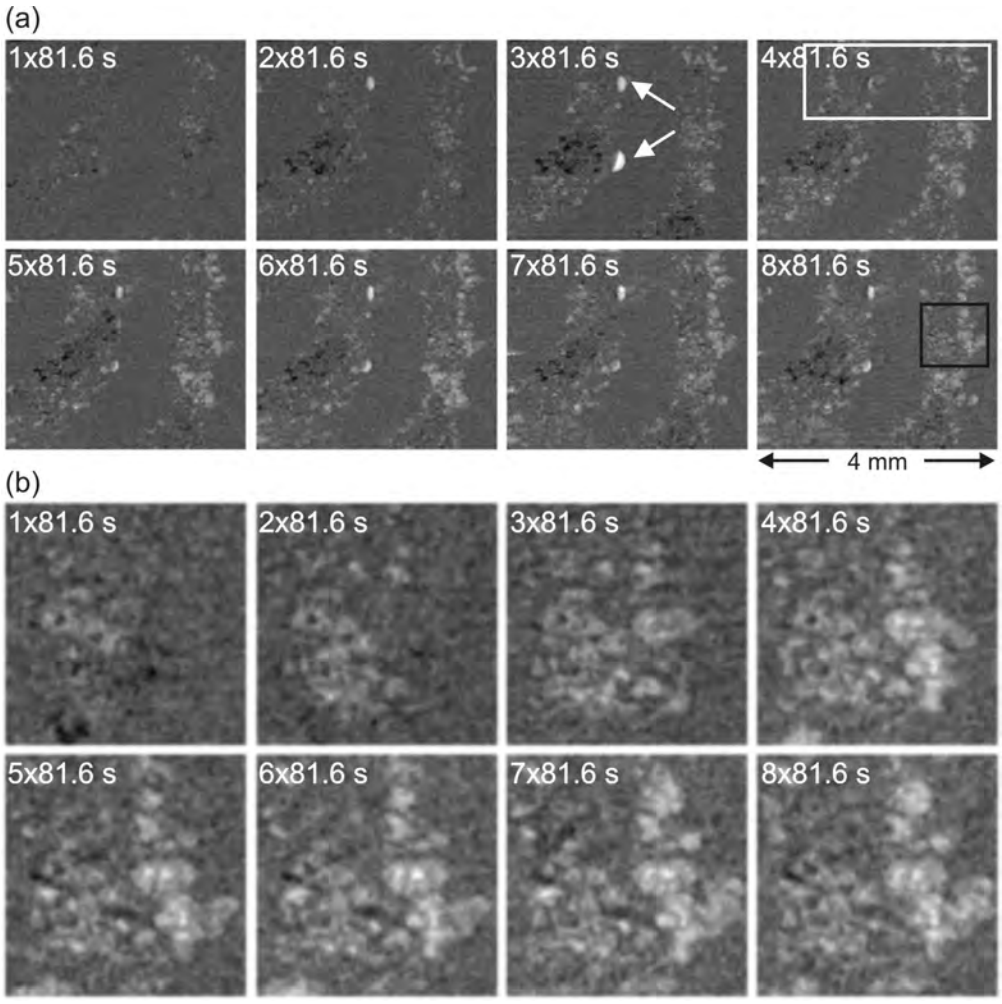

Fig. 6: a) Evolution of liquid water accumulation. The imaged area corresponds to the area marked with a white square in Fig. 3. The time is given in multiples of 81.6 s. The fuel cell was started at an almost dry state. After about 7x81.6 s almost stationary conditions were achieved (the white rectangle denotes the area for the quantification in Fig. 7). b) Corresponding sequence with an enlarged field of view [area marked by a black square in Fig. 6a)].
85x85mm (600 x 600 DPI)

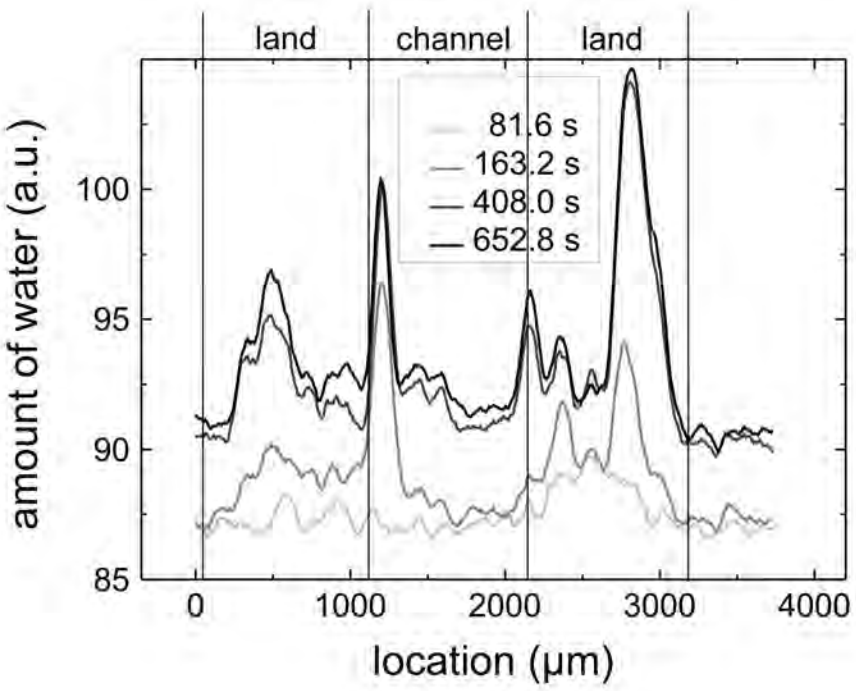

Fig. 7: Quantification of the water distribution along the location marked by a white rectangle in Fig. 6 a) [top right image].
85x67mm (600 x 600 DPI)

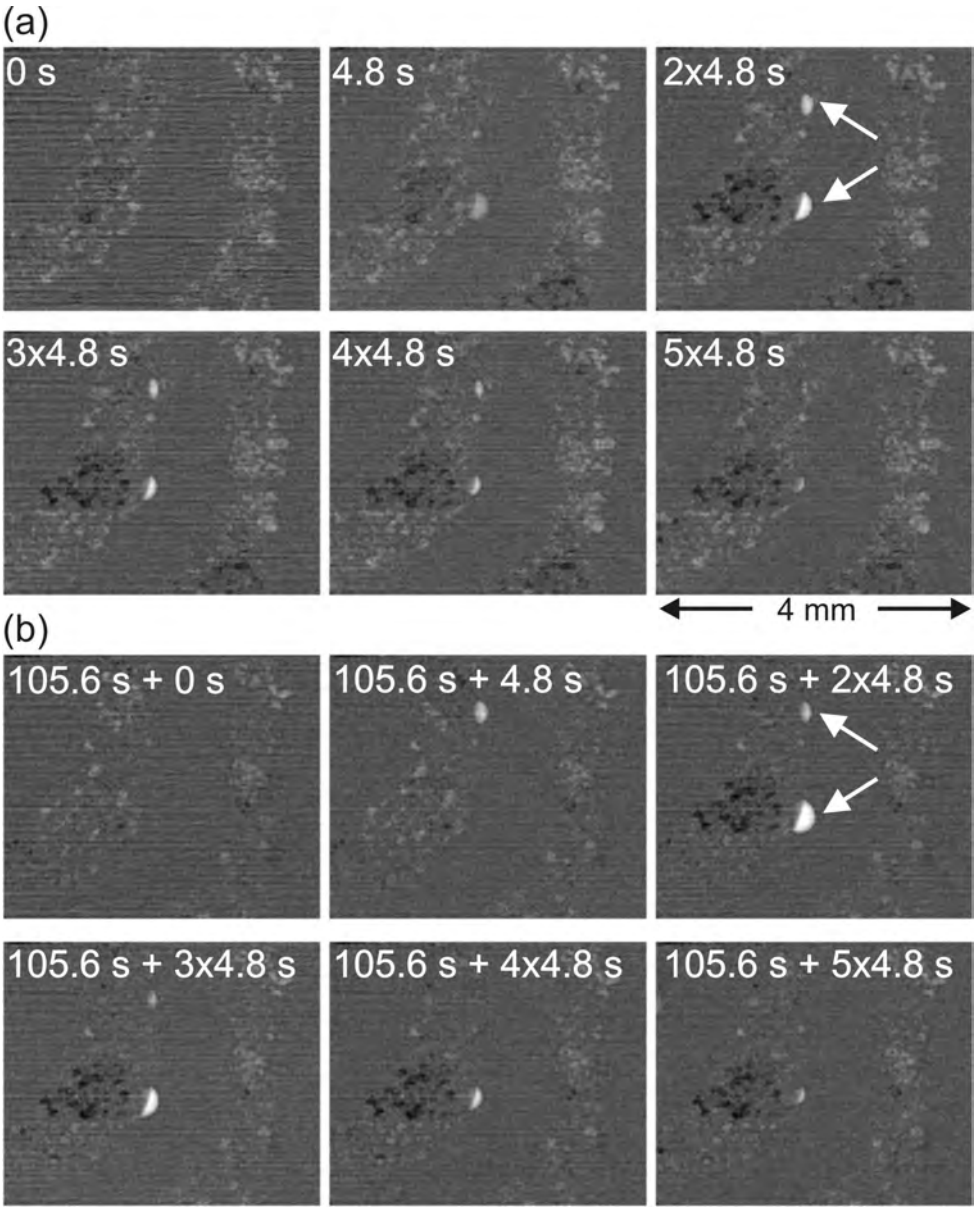

Fig.8: Two sequences showing the eruptive water transport found in Fig. 6 with smaller time steps (4.8s between succeeding images) at the same location. Both sequences show eruptive water expulsion from pores inside the GDL to the cathodic flow field channel. The droplets in the flow field channels are marked by arrows. Sequence b) was measured 105.6 s later. It can be clearly seen that both image series are almost identical, i.e. the eruptive process is periodic.
85x106mm (600 x 600 DPI)

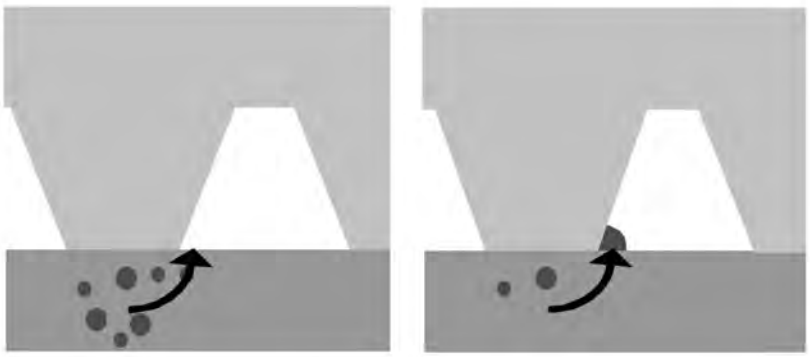

Fig 9: Schematic drawing explaining the eruptive water transport. Water in the GDL is expelled within less than 5 s into the flow field where it forms a droplet.
85x41mm (600 x 600 DPI)

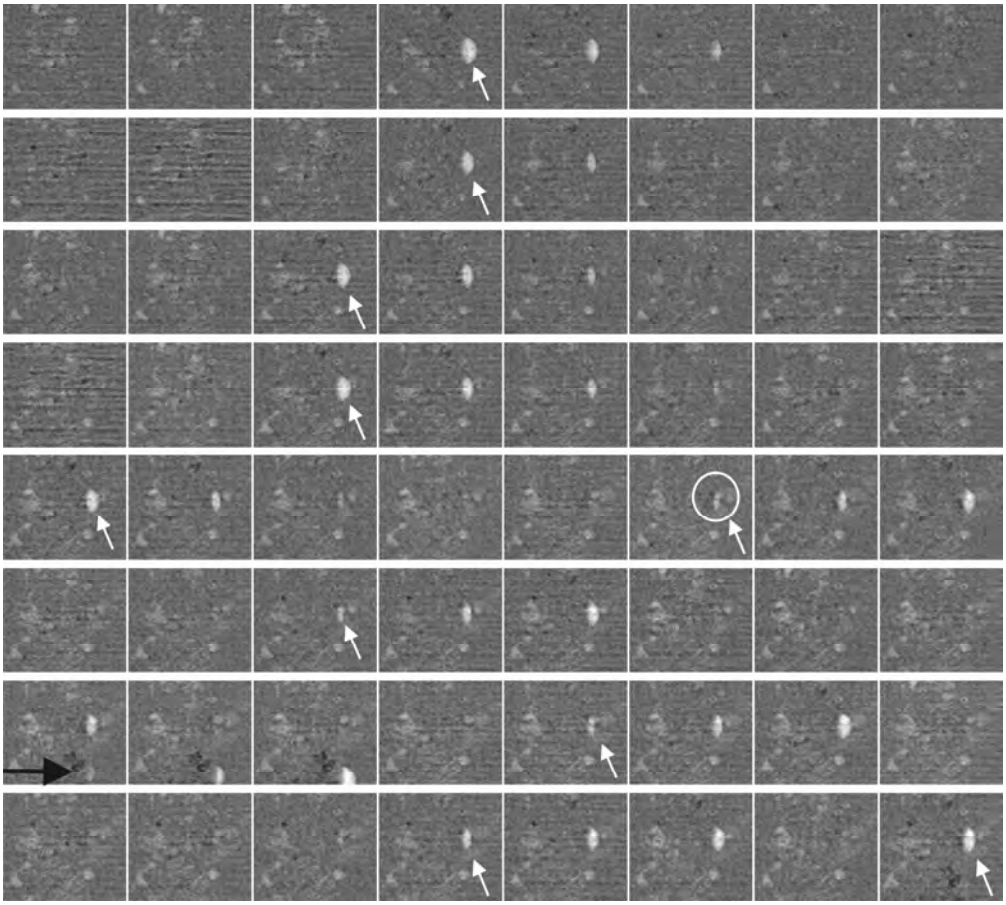

Fig. 10: Eruptive water expulsion from the gas diffusion layer to the cathodic flow field channel: The images show the water distribution in a small area of about 1.4x1.2 mm2. It is a sequence of succeeding images with a time separation of 4.8 s. At the beginning (t = 0 s) the cathodic utilization rate was increased from 95 to 97.5 %. This yields an increase in the repetition rate of the eruptive process. After around 200 s, a second transport channel was opened around 0.5 mm below the first channel (location is marked by a black arrow).
169x152mm (600 x 600 DPI)

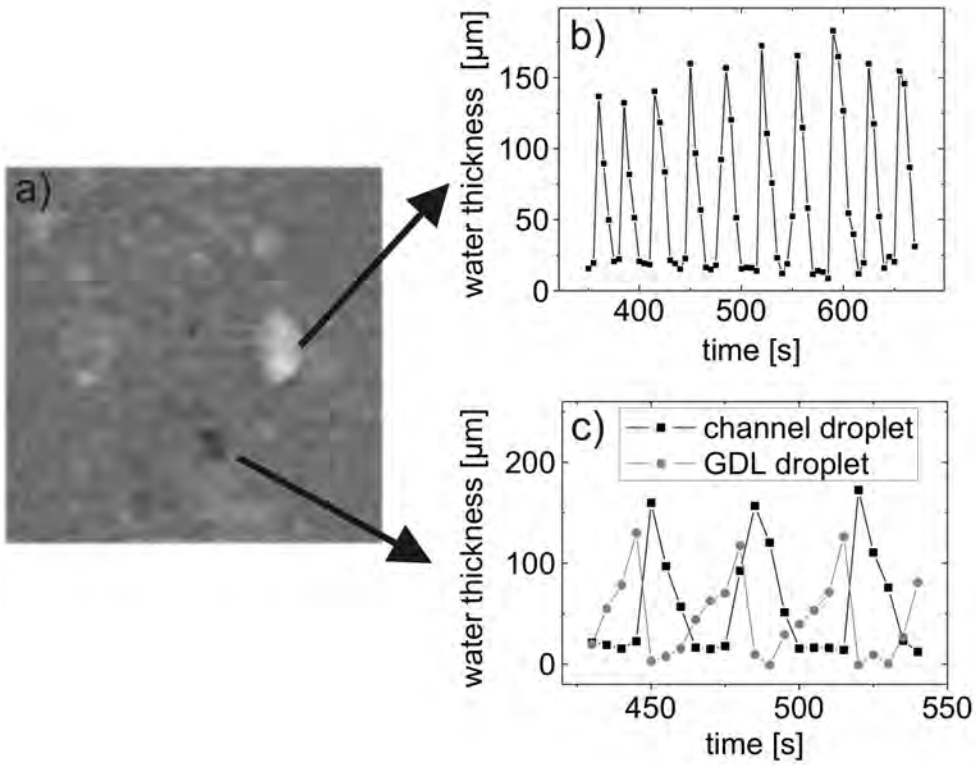

Fig 11: Temporal correlation between water content in the GDL pores and in the corresponding flow field channel (large water droplet). Water accumulations shown in the images in Fig. 10 were quantified for a specific time interval at the two locations marked by arrows. b) amount of water (transmission thickness) at the location of the droplet, c) at a chosen location with in the GDL. For comparison, the corresponding water accumulation at the droplet position is also shown in b). The GDL pore is slowly filled until it is emptied very quickly. At the same time the water droplet forms and is evaporated during the next 10 - 15 sec.
85x71mm (600 x 600 DPI)